AIAA 2002-0438

CFD VALIDATION FOR BASE FLOWS WITH AND WITHOUT PLUME INTERACTION

P.G. Bakker* and W.J. Bannink†
University of Technology Delft, The Netherlands

P. Servel‡ and Ph. Reijasse§
Onera, Meudon, France

Abstract

In the framework of the NATO-RTO-AVT-WG10 entitled "Technologies for Propelled Hypersonic Flight", base flow test cases have been selected for code validation. Concerning the first dataset devoted to base flow-plume interaction at moderate nozzle pressure ratios, the influence of numerical discretization technique and turbulence models are discussed. The multi-dimensional upwind (MDU) discretization technique on unstructured grids applied to the axisymmetric base flow model with an underexpanded jet predicts base pressures that are consistently lower than the experimental values. If no proper conclusions can be drawn from this comparison because of the 3-D model support influence in the experiments, conclusions in relation to the turbulence models and to the axisymmetric results of the other code, the finite-volume technique on multi-block grids (LORE), may be of interest. Concerning the second dataset of a boattailed afterbody flowfield with plume-induced-separation, RANS calculations with transport equations turbulence models reproduce the general organization of the flow, in particular the *free separation* phenomenon with a λ-shock system induced by the jet/external flow interaction. The afterbody wall-pressure profile on the cylindrical part and during the expansion wave is well restituted. But it seems difficult to predict accurately the afterbody wall-pressure profile on the boat-tail because turbulence models have difficulties to reproduce positive pressure gradients. Calculations do not reveal the existence of a singular reflection on the symmetry axis for the recompression *barrel* shock of the propulsive jet, with a Mach disc, as it has been experimentally observed.

Nomenclature

M_∞	free stream Mach number
M_j	jet Mach number
N	ratio of chamber pressure to free stream static pressure
T_t	free stream stagnation temperature
p_t	free stream stagnation pressure
p_{tj}	jet stagnation pressure
p_∞	free stream static pressure
p_e	nozzle exit pressure
p_b	base pressure
p_{bm}	average base pressure
U_∞	free stream velocity

1. Introduction

For the development of the next generation of reusable launchers and re-entry vehicles, one of the critical areas is concerned with the proper modelling of base flow. The low pressures acting on the base region of bodies in supersonic and hypersonic flight cause a significant drag. Due to flow separation from the afterbody followed by mixing with the hot exhaust plume from the nozzle and the reattaching flow at the base thereafter also the heat loading may be considerable. Furthermore, asymmetric effects and unsteady flow phenomena can cause severe side loads on a launch vehicle. Important aspects influencing the base flow physics are e.g. the presence of external flow and the conditions of the exhausting jet (underexpanded or overexpanded), boattailing of the afterbody, base bleed.

Two different experimental data sets meeting the objectives set by the RTO Working Group WG 10 are identified covering a number of the conditions mentioned and (partially) their interactions. Dataset No. 1 (TU Delft) is concerned with the supersonic flow along a cylindrical afterbody with a single operating exhaust jet. Dataset No. 2 (ONERA) considers the flow along an axisymmetric boattailed afterbody also with exhaust jet. Dataset No. 1 deals with overexpanded, accommodated and underexpanded jet flows and Dataset No.2 only with underexpanded jets. Comparing them the influence of boattailing in presence of an exhaust jet may be studied for underexpanding cases, which is of special interest at higher altitudes.

2. Dataset No. 1: Base Flow-Plume Interaction in Supersonic External Flow

* Professor
† Doctor
‡ Research scientist
§ Research scientist

Report Documentation Page

Form Approved
OMB No. 0704-0188

1. REPORT DATE	2. REPORT TYPE	3. DATES COVERED
01 JAN 2006	**N/A**	**-**

4. TITLE AND SUBTITLE	5a. CONTRACT NUMBER
CFD Validation For Base Flows With And Without Plume Interaction	5b. GRANT NUMBER
	5c. PROGRAM ELEMENT NUMBER
6. AUTHOR(S)	5d. PROJECT NUMBER
	5e. TASK NUMBER
	5f. WORK UNIT NUMBER
7. PERFORMING ORGANIZATION NAME(S) AND ADDRESS(ES) **University of Technology Delft, The Netherlands**	8. PERFORMING ORGANIZATION REPORT NUMBER
9. SPONSORING/MONITORING AGENCY NAME(S) AND ADDRESS(ES)	10. SPONSOR/MONITOR'S ACRONYM(S)
	11. SPONSOR/MONITOR'S REPORT NUMBER(S)

12. DISTRIBUTION/AVAILABILITY STATEMENT
Approved for public release, distribution unlimited

13. SUPPLEMENTARY NOTES
See also ADM001860, Technologies for Propelled Hypersonic Flight (Technologies des vols hypersoniques propulses). , The original document contains color images.

14. ABSTRACT

15. SUBJECT TERMS

16. SECURITY CLASSIFICATION OF:			17. LIMITATION OF ABSTRACT	18. NUMBER OF PAGES	19a. NAME OF RESPONSIBLE PERSON
a. REPORT	b. ABSTRACT	c. THIS PAGE			
unclassified	**unclassified**	**unclassified**	**UU**	**16**	

2.1 *Description of Model Configuration*

The selected geometry is an axisymmetric blunted cone cylinder. The conical forebody and the cylindrical afterbody are about the same length. The model is supported at the lower side of the aft part and has a free base, see Fig. 1. From the center of the base a nozzle protrudes, its outer shape is a circular cylinder. The inner nozzle is conical with a divergence of 15 deg. The inner exit diameter of the nozzle is 16.4 mm, being about 1/3 of the model base diameter. The nominal jet Mach number was chosen to be 4. The conical forebody has a semi-apex angle of 11 deg. and a nose radius of 7.5 mm. The total length of the model is 186.81 mm and the length of the cylindrical afterbody is 90 mm.

Along the afterbody 10 pressure taps are provided. In the upperpart of the base 17 taps are foreseen. To increase the measuring resolution and because of limitations in manufacturing the taps at the base are provided in three rays. The location of the taps is shown in Fig. 2.

The model is positioned at zero incidence in a uniform supersonic free stream.

The test set-up enables the investigation of the flow field along the model with a single operating exhaust jet. In the interaction region between jet and external flow behind the base a turbulent mixing layer, a recirculating region and a shock system (plume shock, barrel shock, Mach disc) are formed.

2.2 *Description of Experiment*

In order to ascertain that the boundary layer approaching the base of the body is turbulent it is tripped at 38 mm from the nose of the model.

The measurements are made in the transonic/supersonic wind tunnel TST27, test section 27 cm x 28 cm, of the Aerospace Department of the Delft University ot Technology. Tests were performed at free stream Mach numbers of 1.96 and 2.98 and at stagnation pressures p_t = 2.06 bar and p_t = 5.75 bar, respectively, with an accuracy of 1 %. The stagnation temperature T_t = 285 ± 2 K. The jet stagnation pressures ranged from p_{tj} = 3.5 bar to 100 bar, with an accuracy of 1.5 %. The Mach number at the nozzle exit was measured to be M_j = 3.96 ± 0.02.

The Reynolds numbers based on the model length are $5.1 \cdot 10.^6$ and $8.7 \cdot 10.^6$ at free stream Mach numbers of 1.96 and 2.98, respectively.

The distinction between underexpanded and overexpanded jets cannot be given by the ratio of the jet exit pressure p_e to the free stream static pressure p_∞. This is because p_∞ cannot be considered as the ambient pressure near the nozzle exit. Therefore, as a measure for the status of the exhausting jet, the ratio of p_e to the mean base pressure p_{bm} has been taken. The base pressure is close to ambient pressure. As will be seen the ratio p_e/p_{bm} yields a good appreciation for the jet status: $p_e < p_{bm}$ indicates overexpansion and $p_e > p_{bm}$ underexpansion.

For a complete report of the experiments one is referred to Refs. 1, 2 and 3. In the present article only those cases will be considered that are of interest for the validation of CFD capacity. In Table 1 a selected test matrix is given.

No	M_∞	p_∞ (bar)	p_{tj} (bar)	N= p_{tj}/p_∞	p_{bm}/p_∞	p_e/p_∞	p_e/p_b
1	2.98	0.1613	31.3	194.1	0.244	1.348	5.518
2	2.98	0.1618	no jet	----	0.326	------	------
3	1.96	0.2830	no jet	----	0.513	------	------
4	1.96	0.2830	3.65	12.9	0.439	0.090	0.204
5	1.96	0.2830	12.45	44.0	0.299	0.306	1.022
6	1.96	0.2830	49.2	173.9	0.363	1.208	3.332

Table 1 : Test matrix for validated cases, M_j = 3.96

The dynamic behaviour of the base flow has been tested in two series of measurements at free stream Mach numbers of M_∞ = 1.96 and 2.98, each series at several jet stagnation pressures. During these tests the base pressures were measured with high sensitive piezo resistive transducers. The pressure signals showed a noise rubble of a few percent of the mean static base pressure with a frequency of 10 kHz or less.

2.3 *Computational Methods*

The results of two CFD codes will be discussed. The first code is based on a multi-dimensional upwind method on unstructured grids (Refs. 4 and 5). The code has been applied on the flow around the model without support, thus on an axisymmetric flow problem. Naturally, this will involve disagreement with the experimental results. Four turbulence models are considered (see section 2.3.1).

The second code (Ref. 5) is based on a cell-centered finite-volume method using the flux-difference-splitting scheme of Van Leer. Structured multiblock grids are employed and two turbulence models are applied. In this simulation the flow around the 3-D configuration including the support effect, as well as an axisymmetric configuration has been computed.

2.3.1 *Multi-Dimensional Upwind method (MDU)*

The MDU method is decribed in great detail in Van der Weide's Ph.D thesis, Ref. 4 and its references. It is a well established method for scalar convection problems for which it leads to improved schemes with compact stencils. The method has been generalized by Van der Weide to non-commuting hyperbolic systems and it is constructed such that for any decoupled equation of the system it automatically reduces to the scalar distribution scheme on which it is based. The inviscid part of the Navier-Stokes equations has been discretized by a nonlinear monotone, second-order, multi-dimensional upwind scheme, the PSI-scheme. The Petrov-Galerkin finite element interpretation of the scheme allows a straightforward discretization of the viscous terms. The discretization of these terms on linear elements through integration by parts condenses

to the Galerkin method. The time integrator is the backward Euler method.
The governing equations for the turbulence models are solved in a fully coupled manner on the explicit level, but its off-diagonal entries are ignored in the Jacobian matrix of the backward Euler method. This technique appears to be more stable than the fully coupled approach. The convection terms of the turbulent transport equations are discretized with the second-order PSI-scheme.
The turbulence models used are the following one-equation or two-equation models:

- Spalart-Allmaras: an empirical one-equation model;
- k-ω: a two equation model;
- BSL: the baseline two-equation model, which is a blending of the k-ε and k-ω models;
- SST: the two-equation shear stress transport model.

The computations with the MDU method have been performed for Case No.1 of Table 1. A hybrid structured/unstructured approach (Ref. 7) is used to generate a coarse and a fine grid. The coarse version (Fig. 3) has 15,505 nodes of which approximately 12,000 are located in the structured part near the walls. The unstructured part is much too coarse to predict the base flow accurately. Therefore, a very fine grid consisting of 119,519 nodes is generated in the base region, see Fig. 4. To investigate the solution in this region in even more detail it has been computed separately on a 925 x 481 triangulated structured grid, which is on the average 5 times finer in each co-ordinate direction than that of Fig. 4.

2.3.2 *Finite-Volume Flux-Difference method (LORE)*
The LORE computational method (Ref. 6) is a full Navier-Stokes solver for high temperature flows including chemical and thermal nonequilibrium effects. The governing equations are discretized based on a cell-centered finite volume method. It is provided with second-order accurate upwind discretizations according to the flux-difference splitting scheme of Van Leer. Higher order spatial discretizations are obtained with Monotone Upstream Schemes for Conservation Laws (MUSCL), an interpolation technique with a Van Albada limiter to suppress spurious oscillations at discontinuities. Structured multi-block grids are used to compute flows around complex geometries.
Two turbulence models of the two equation type are applied in the present application of the LORE code (see also Ref. 8):

- k-ω;
- SST, of which two versions are used: SST-0 and SST-1, without and with compressibility correction, respectively.

The computations have been made for Cases No's 2 - 6 of Table 1. Two multi-blocked structured grids are generated: one grid is axisymmetric containing only the model and the other grid is three-dimensional, containing model and its wind tunnel support. In both cases a coarse and a fine grid is used. The fine grid is obtained by a refinement of the coarse grid by a factor 2 in the co-ordinate directions. The coarse axisymmetric grid consists of a total of 17,404 cells and the fine grid 4 times as much, 69,616 cells. In the 3-D case these numbers are 353,026 and 2,824,208, respectively. Figs. 5 and 6 show the coarse grids for the 3-D configuration. The wind tunnel wall is represented as circular tube with a diameter of 270 mm, being the height of the actual test section. The outflow boundary is chosen at 400 mm behind the model nose, there the flow is supersonic and consequently no boundary conditions need to be imposed.

2.4 *Results*

2.4.1 *Results of the MDU method*
Computational and experimental results for Case No.1 (axisymmetric flow) of Table 1 are shown in Figs. 7 and 8. Fig. 7 represents the pressure distribution on the cylindrical part of the model; it may be observed that the boundary layer thickness has some influence near the edge of the base (compare the turbulent and laminar solutions). The pressure distribution along this part is mainly determined by the inviscid solutions (Ref. 5). All results are nearly identical and fit the experimental data very well, apparently no influence of the model support is felt there.
In Fig. 8 the computed pressure distributions at the base are compared with the experimental values. The laminar distribution may only serve as illustration, since it is not realistic in the practice of this application. In particular Fig. 8c shows this. On the triangulated structured grid the laminar solution is highly unsteady. Numerically Von Karman vortex sheets are observed. Due to numerical difusion the laminar solutions on the coarse and fine grid (Fig. 8a, 8b) are steady (see Ref. 4).
All solutions on the coarse grid are not grid converged, as shows the sequence in Fig. 8. The solution obtained with the Spalart-Allmaras model on the fine grid is identical to that computed on the triangulated structured grid, compare Figs. 8b and 8c. Consequently, this solution is grid converged. However, it is clear that the solutions of the two-equation models on the fine grid are not grid converged, since the base pressures on the triangulated structured grid shown in Fig. 8c are 25 to 50 % higher. All turbulence models predict the base pressure too low compared with the experimental values. This observation is even more cumbersome if one realizes that the influence of the model support is to decrease the base pressure, see Ref. 9.
In case of the Spalart-Allmaras turbulence model much of the difference may be explained by the deficiency of the turbulence model itself, this model shows grid convergence whereas for the two-equation models the solutions cannot be assumed to be grid converged.

However, also for the latter models the situation is not evident either. It might be possible that on finer grids the base pressure increases further. Furthermore, it is not at all clear what is the effect of imposing the entire solution (interpolated from the fine grid solution) on the flow boundaries of the triangulated structured grid in the base region. Ref. 4 speaks of strong changes of the solution in the interaction region so that a wrong solution is imposed there.

On the triangulated structured grid, Fig. 8c, the k-ω model predicts a significantly higher base pressure than the BSL and SST models, whose formulations are almost identical to the k-ε model in this part of the flow field.

The correct prediction of the base flow characteristics requires extremely fine grids, in particular for the two-equation models. As the refinement of the grid increases the relative difference between the results increases also, although they remain quite close to each other, see Fig. 8b. The result obtained with k-ω on a very fine structured grid (Fig. 8c) is still increasing. It is believed in Ref. 4 that the base flow characteristics cannot be predicted accurately by eddy-viscosity turbulence models. Apparently this is not the case here as long as sufficiently fine grids are used. Ref. 4 states such a conclusion might be a coincidence and that more cases should be computed for a decisive conclusion.

2.4.2 *Results of LORE*

Case No. 2: $M_\infty = 2.98$, no exhaust jet

The influence of grid (coarse/fine) and of turbulence models (k-ω, SST-0, SST-1) will be discussed for the axisymmetric case with plume off.

The axisymmetric flow topologies in the base region are shown in Fig.9. Like the MDU method the laminar results are included as a comparison. The different turbulence models show basically similar topologies. The number of vortices and their location is almost the same. There is influence on the size of the vortex near the base, this will of course have its effect on the base pressure distribution. The grid size does not seem to give great topological differences with the exception of the SST-0 model. The solutions are shown to be grid independent in Ref. 10, where also the convergence of the solutions is proved.

Fig. 10 contains the base flow topologies of the 3-D configuration (model with support) computed on the coarse mesh (353,026) cells. The number of vortices obtained with the various turbulence models is different, i.e. compare the upper base region for k-ω and SST and the lower region for all turbulence models.

The surface shear stress computed with the SST-1 model is compared to the experimental oil flow visualization in Fig. 11. The agreement ie surprisingly good, not only on the model itself but also on the support near the junction with the model where the separation lines are very well simulated.

Finally, for Case 2, the radially distributed base pressures are presented in Fig.12. Disregarding the laminar distribution which is not well understood, one may conclude that the discrepancy between numerical results of the different turbulence models is not very large, particularly not in the 3-D case. In addition, it may be noticed that the presence of the support apparently decreases the base pressure. This is in agreement with the experimental results of Ref. 9 where the influence of aft fin locations were studied on the base pressures of axisymmetric models in supersonic flow. The 3-D simulations made with the SST-1 model (with compressibility correction) are closest to the experimental data. SST-1 together with the fine mesh (2) shows that the pressure level compared to the SST-0 solution is maintained but that the resolution at the edge of the base is improved.

Cases No. 3 to 6: $M_\infty = 1.96$, with jet exhaust

Since the results in the plume-off case using the SST-1 turbulence model showed the best agreement with the experimental data the Cases No's 3 to 6 are computed with SST-1 only. The axisymmetric computations are performed on two meshes to show mesh independence. Because of this and the CPU time consuming character of the 3-D simulations only the coarse mesh is used for the configuration with support.

Fig. 13 illustrates the difference in base flow topology. The plume-off case may be compared to that of Case No. 2 at M_∞ =2.98 shown in Fig. 10, which is also calculated with SST-1. The number and location of vortices is different; due to the higher free stream Mach number the more intense shear layer emanating from the edge of the base appears to have its effect on the base flow topology.

The radial base pressure distribution of all flow cases is presented in Fig. 14. The trend for the plume-off case is similar to that at $M_\infty = 2.98$: as may be expected the axisymmetric pressures do not agree with the experimental results and the 3-D simulations are close to the measured values.

The 3-D overexpanded and accommodated jet computational data are quite satisfactory, although the constant character of the distributions disappears at higher jet pressures. The maxima in the pressure distributions may indicate a reattaching flow at the base. However, there is no strong evidence in the streamline patterns of Fig. 13. All cases with jet exhaust show basically similar flow topologies.

The nice agreement with experiments seems to decrease for higher pressure ratios, since the pure underexpanded jet at N = 173.9 causes all computed base pressures to give an underestimation of about 25 % to the measurements.

An explanation for the discrepancy may be found in the grid size. As can be observed in Fig. 6 the shear layer region between exhaust and ambient flow does not have a very dense grid point distribution. Considering Fig. 14 it appears that the difference between the axisymmetric results on the coarse and the

fine grid increases with increasing chamber pressure. The fine mesh contains more grid points and therefore a better capturing of the gradients is achieved, leading to a better simulation of the base flow. The coarse grid shown in Fig. 6 may be suited to compute the plume-off and overexpanded cases because the gradients in the shear layer are not so large. So, again, as in the application of the MDU method, the conclusion may be that finer grids should be used to predict the base flow more accurately.

2.5 *Conclusions*

The multi-dimensional upwind (MDU) discretization technique on unstructured grids applied to the axisymmetric base flow model with an underexpanded jet predicts base pressures that are consistently lower than the experimental values. Naturally, no proper conclusions can be drawn from this comparison because of the 3-D model support influence in the experiments. However, conclusions in relation to the turbulence models and to the axisymmetric results of the other code, the finite-volume technique on multi-block grids (LORE), may be of interest.

The conclusions are summarized in the following.

- The MDU code needs extemely fine meshes to obtain a grid converged solution.
- With the exception of the one-equation Spalart-Allmaras model the other turbulence models applied (k-ω, SST, BSL) show almost no difference in results on the coarse and fine grids.
- Only on the very fine triangulated structured grid in the base region the k-ω model predicts a significantly higher base pressure than the BSL and SST models.
- The Spalart-Allmaras model is unable to predict the physical phenomena in the base region correctly.
- The computations made with LORE have shown that, in agreement with experiments, the presence of a model support causes a decrease of the base pressure.
- In the plume-off case LORE does not show a significant effect of grid size on the results. Grid independence exists also in the axisymmetric plume-on cases, where the 3-D computations are only made on a coarse grid.
- From the turbulence models used (k-ω, SST-0, SST-1) the LORE 3-D results show the best base pressure prediction for the SST-1 model (with compressibility correction).
- Very good agreement with the experimental data is obtained for the plume-off, overexpanded and jet-accommodated flow cases. The results for the underexpanded jet are underpredicted.
- Qualitative comparison between the axisymmetric results of MDU and LORE reveals that MDU underpredicts the base pressures considerably with respect to LORE.
- Among each other both methods show large differences in base flow topologies.

3. Dataset No. 2: Plume-Induced Separation on a Boattailed Afterbody in Supersonic External Flow

3.1 *Model Configuration and Stagnation Conditions*

Tests have been performed in the continuous atmospheric research wind tunnel S8Ch of Onera at Chalais-Meudon Center. The wind tunnel is equipped with two planar half-nozzles, producing a uniform Mach 2 flow in a 120mm-side square test section. The stagnation conditions of the external flow are : p_t = 0.975bar for the pressure, and T_t = 298K for the temperature. The axisymmetric model is mounted at the extremity of a centerbody fixed in the settling chamber. The afterbody geometry (Fig. 15) consists in a 9.5deg.-conical boattail with a length of 31.5mm. The external diameter of the model is D = 30mm. The external Mach number of the unperturbated incoming flow is M_∞ = 1.94. The length of the centerbody from the wind tunnel throat to the model boattail is L = 212.5mm. The Reynolds number based on the length L is 2.65 10^6. The model is equipped with a 10deg.-conical nozzle fed by dessicated air. The stagnation temperature of the jet is T_{tj} = 298K. The exit diameter of the model nozzle is 14.9mm and the exit Mach number on the centerline is M_j = 1.75. The stagnation pressure of the jet is p_{tj} = 7.75bar.

3.2 *The Onera Laser Doppler Velocimetry (LDV) Bench*

The LDV system, which was operated in the forward scatter mode, has been used in its two-component version. The light source is a 15W argon ion laser operating at 8W for all lines. The crossing of dichroic plates allows selection of the green and blue lines, their wavelengths being 0.5145 and 0.4880nm, respectively. Each beam is divided when it crosses beam splitters. The two resulting monochromatic beams are then focused in order to create an interference fringe pattern. The diameter of the probe volume, constituted by the two fringe systems, is 200μm and the focal distance is 1m. The blue and green fringe spacings are 13.165 and 12.684μm, respectively. Frequency shifting at 15MHz is used to discriminate the direction of the measured velocity component. The external stream is seeded with sprayed olive oil by the means of a movable tube placed in the settling chamber of the wind tunnel. The seeding of the jet is ensured by submicron (0.5μm diameter) magnesium oxide (MgO) particles injected far upstream of the model nozzle throat.

3.3 *Computational Methods*

3.3.1 *Presentation of the NASCA code*

The numerical simulations presented below have been performed with an axisymmetric version of the Reynolds Averaged Navier-Stokes (RANS) NASCA

research code (Ref. 11). In this code, we solve the full system of Navier-Stokes equations for perfect gas by means of a finite volume technique in which the time-averaged Navier-Stokes equations, in their conservative form, are integrated on each cell surrounding each calculation point with a spatially second-order-accurate method.

This is an implicit first-order-accurate in time code using an ADI-type (Alternating Direction Implicit) factorisation for each direction in space while inverting the matrix of the system. The numerical procedure described in Ref. 11 for the scheme of the NASCA code uses a classical central-difference approximation for the diffusion terms and a high-resolution TVD (Total Variation Diminishing) shock-capturing method for the inviscid part of the Navier-Stokes equations (i.e. the non-linear Euler equations).

Thus, we evaluate the convective fluxes at the interfaces between the integration cells in an upwind manner for the Steger and Warming flux-vector splitting (based on the sign of the eigenvalues of the Jacobian matrix of the convective operator). Then, the spatially first-order-accurate implicit part of the convective terms uses an approximate Riemann solver due to Roe while the spatially second-order-accurate explicit part is an extension of the Osher and Chakravarthy scheme to a non-uniform and non-orthogonal grid.

In order to solve the fully turbulent Navier-Stokes equations, the eddy viscosity related to the turbulent shear and normal stresses by the Boussinesq hypothesis (analogy of the Reynolds tensor to the viscous tensor) has to be calculated. For this purpose, turbulence models of two types are proposed (Ref. 12):

- the algebraic Baldwin-Lomax turbulence model, based on the mixing-length theory,
- the two transport equations k-ε turbulence model due to Chien.

In this last case, in order to calculate the eddy viscosity, the transport equations for the turbulent kinetic energy k and its dissipation rate ε are solved thanks to the same method as mentioned above for the mean flow variables (see Ref. 13 for more details).

3.3.2 *Grids, boundary conditions and computational procedure*

The computational grid for the following numerical calculations contains 265 points in the X-direction and 190 points in the Z-direction, with mesh refinements in directions perpendicular to the afterbody and base walls determined after a careful analysis of spatial convergence, especially for the transverse grid distribution on the base and on the boat-tail (Ref. 12).

The upwind and the upper boundaries of the calculation grid are considered as supersonic inlets where all the variables of the flow are imposed, especially the boundary layers of the external flow at X / D = -2, far upstream from the base which is located at X / D = 0, and the internal propulsive jet at the nozzle lip, both evaluated from the experiments (Ref. 12). The downstream boundary constitutes a supersonic outlet where all the variables are extrapolated from the interior of the mesh. The lower boundary is treated with an axial symmetry condition while the afterbody and the base walls, where $k = \varepsilon = 0$, have adiabatic wall conditions ($u = w = \partial P/\partial N = \partial T/\partial N = 0$).

A steady solution was reached through the solution of the pseudo-unstationary Navier-Stokes equations and the convergence in time is obtained in 8000 iterations for this case of propelled afterbody supersonic flow. This convergence has needed about 3 hours on Cray YMP using the Baldwin-Lomax turbulence model and 5 hours using the Chien k-ε model.

3.4 *Results*

The Mach number levels obtained from the results of the Navier-Stokes calculations with the NASCA code when using the Baldwin-Lomax turbulence model are shown in Fig. 16, where the general organisation of the flow around the propelled boat-tailed afterbody can be seen and is equivalent to the flow organisation obtained with the Chien k-ε model. Upstream of the boat-tail, the external supersonic flow is quite uniform along the cylindrical part of the afterbody, except the boundary layer near the wall.

Then, the angle of the conical boat-tail induces a deflection of the external flow and the point at the beginning of the boat-tail (X / D = -1) constitutes the origin of a centred expansion wave, visible on Fig. 16. Correlatively, the external wall-pressure suddenly decreases, which favours the jet expansion ratio. This boat-tail angle induces such a high nozzle expansion ratio so that the underexpanded internal jet expands largely at the nozzle exit. There results an obstacle effect for the external stream that induces a deflection of this last flow upon the conical part of the afterbody, accompanied by a strong shock-wave and a separation of the afterbody boundary layer. A second oblique shock issuing from the confluence region between the the external flow and the propulsive jet is joining the former separation shock. Thus, this plume/afterbody flowfield is characterized by a λ-shock system constituted by the separation shock and the confluence -or trailing- shock. In fact, we can notice here a *free* separation occurring on the afterbody boat-tail induced by the pluming of the jet.

For the jet, the flow well separates at the nozzle lip, undergoing a centred expansion wave, as we can observe in Fig. 16. In this case of base flow with plume-induced separation, the separated zone also called *dead-air* region, consists in a recirculating bubble enveloping the base and the ending part of the boat-tail. This recirculation zone is in fact barely visible in Fig. 16 due to its small size.

The trailing shock of the jet, named *barrel* shock because of its shape, reflects downstream in a regular manner on the symmetry axis. Downstream from the confluence region between the two co-flowing

streams, the external flow and the propulsive jet are contiguous on each side of a common boundary along which a viscous wake develops, a shear layer also observable in Fig.16.

Fig. 17 shows the repartitions of static pressure along the walls of the cylindrical and conical parts of the afterbody, upstream from the base which is at X / D = 0. The results of the calculations executed with the algebraic Baldwin-Lomax turbulence model (in solid line) and with the two-transport-equations Chien k-ε model (in dashed line) are drawn in comparison to the experimental pressure values, (see symbols in Fig. 17). The experimental base pressure are given thanks to four pressure holes distributed in each quadrant.

The simulated profiles seem in good agreement with the experimental values on the cylindrical part of the afterbody and for the brutal expansion at the beginning of the boat-tail. We note that the base pressure value, given in Fig. 17 at X / D = 0, is well predicted, but the calculations, with both turbulence models and particularly the k-ε one, do not fit satisfactorily the afterbody wall-pressure profile through the interaction. Calculations anticipate the beginning of the compression on the middle of the boat-tail, and give more gentle evolution of pressure profiles with less steep pressure slopes. Thus, the numerical simulations over-predict the abscissa of the separation point (X / D = -0.24 and -0.35, for respectively the Chien k-ε and Baldwin-Lomax turbulence models) compared to the experimental value (X / D = -0.4). The simplest model (Baldwin-Lomax) presents curiously the smallest over-prediction but is better adapted for separated flows than the Chien model for which, moreover, the turbulent quantities have not been precisely initialized near the wall from the experimental values.

The radial distribution of field properties are shown in the three last figures which give the mean axial velocity profiles (Fig. 18), the mean radial velocity profiles (Fig. 19) and the turbulent shear stress profiles (Fig. 20). The first four stations of the three figures (the three profiles upstream from the base : X / D = -1, -0.33 and -0.13, and the profile at the base : X / D = 0) repeat what has been noticed for the static wall pressure : if the calculated profiles seem in agreement with the experimental values away from the wall, calculations delay the apparition of the separated zone, especially with the Chien k-ε turbulence model.

In the dead-air region just downstream from the base, at X / D = 0.13, the discrepancies of the turbulence models are visible in the size of the recirculation zone and in the levels of mean and turbulent quantities (Figs. 18-20). Firstly, this is a consequence of what happens upwind in the external flow around the afterbody, i.e. an underprediction of the size of the separated region due to the λ-choc. Secondly, there is a lack of information on the nozzle boundary layer, which induces an uncertainty in the initialization of the internal flow. The last five stations of Fig. 18-20 show a better agreement between experimental measurements and numerical simulations, except for the prediction of the position of the viscous shear layer separating the external flow and the propulsive jet. The jump in the profiles of the three quantities (u, w and u'w') is situated in the calculation results at a lower altitude than in the experiments. It is correlated to the fact that the results of numerical simulations performed with the Navier-Stokes NASCA code have never predicted the Mach disk seen in the experimental visualisations (Ref. 12). This can been observed in the last picture of Fig. 18 where the experimental profile of the axial velocity u at X / D = 3.5 presents a jump near Y / D ~ 0.32 which reveals the subsonic area downstream from the Mach disk, this singular reflection of the barrel shock not existing on the results of the calculations (Figs. 16,18). The non-restitution of the Mach disk pattern could be explained through a difference in the way of establishing the two flows between experiments and calculations: while, in the simulations, the two flows, the external one and the internal jet, are calculated together, in the wind tunnel, the jet starts after having firstly established the main flow.

3.5 *Conclusion*

RANS calculations with transport equations turbulence models can give a good description of the afterbody flowfield in plume-induced-separation configurations. In particular they reproduce the *free separation* phenomenon with a λ-shock system induced by the jet/external flow interaction :

- The general organization of the flow is well reproduced, in particular the viscous boundary and shear layers, the expansion-compression waves and the system of shocks.
- The afterbody wall-pressure profile on the cylindrical part and during the expansion wave is well restituted.

But it seems difficult to predict accurately the following flow field details of such a plume induced separation :

- The afterbody wall-pressure profile on the boat-tail is not well predicted because turbulence models have difficulties to reproduce positive pressure gradients.
- Calculations do not reveal the existence of a singular reflection on the symmetry axis for the recompression *barrel* shock of the propulsive jet, with a Mach disc, as it has been experimentally observed.

References

1. Bannink, W.J., Bakker, P.G. and Houtman, E.M., FESTIP Aerothermodynamics: Experimental Investigation of Base Flow and Exhaust Plume Interaction, Memorandum M-775, Aerospace Engineering, Delft University of Technology, 1997.
2. Bannink, W.J., Houtman, E.M. and Bakker, P.G., Base Flow/Underexpanded Exhaust Plume Interaction in a Supersonic External Flow, AIAA 8th Internat. Space Planes and Hypersonic Systems

and Technology Conf., Norfolk VA, 1998, Paper AIAA-98-1598.
3. Bannink, W.J., Proot, M.M.J. and Donker Duyvis, F.J., Final Experimental Results FESTIP Aerothermodynamics Phase 2 (1998-1999),Critical Point Analysis, ESA Contract 11.534/95/NL/FG, 2000.
4. Van der Weide, E., Compressible Flow Simulation on Unstructured Grids Using Multi-Dimensional Upwind Schemes, Ph.D thesis, Aerospace Engineering, Delft University of Technology, 1998.
5. Houtman, E.M., Van der Weide, E., Deconinck, H. and Bakker, P.G., Computational Analysis of Base Flow/Jet Plume Interaction, Proc. 3d European Symp. on Aerothermodynamics for Space Vehicles, ESA SP-426, pp 605-612, 1998.
6. Walpot, L.M.G.F., LORE: a 3-D Navier Stokes Solver for High Temperature Chemical and Thermal Nonequilibrium Gas Flows, Ph.D thesis in preparation, Aerospace Engineering, Delft University of Technology.
7. Carette, J.-C, Adaptive Unstructured Mesh Algorithms and SUPG Finite Element Method for High Reynolds Number Compressible Flows, Ph.D thesis, Université Libre de Bruxelles, 1997.
8. Ottens, H.B.A., Gerritsma, M.I. and Bannink, W.J., Computational Study of Support Influence on Base Flow of a Model in Supersonic Flow, AIAA 15th AIAA Computational Fluid Dynamics Conf., Anaheim CA, 11-14 June 2001, Paper AIAA-2001-2638.
9. Heyser, A. Maurer, F. and Oberdörffer, E., Experimental Investigation on the Effect of Tail Surfaces and Angle of Attack on Base Pressure in Supersonic Flow, In: The Fluid Dynamic Aspects of Ballistics, AGARD CP 10, 1966.
10. Ottens, H.B.A., FESTIP Aerothermodynamics: A Computational Study of Base Flow and Exhaust Plume Interaction, Master's thesis. Aerospace Engineering, Delft University of Technology, 2000.
11. Benay R. and Servel P., Applications d'un code Navier-Stokes au calcul d'écoulements d'arrière-corps de missiles ou d'avion. La Recherche Aérospatiale, 1995, n°6, pp. 405-426.
12. Benay R., Corbel B., Reijasse Ph. and Servel P., Etude expérimentale et numérique d'un arrière-corps muni d'un rétreint avec jet propulsif fortement éclaté. ONERA, RTS n° 37/4361 AY (January 1997).
13. Benay R. and Servel P., Modélisation de l'écoulement autour d'un arrière-corps d'avion de combat. ONERA RSF n° 24/4361 AY (September 1993).

Figures

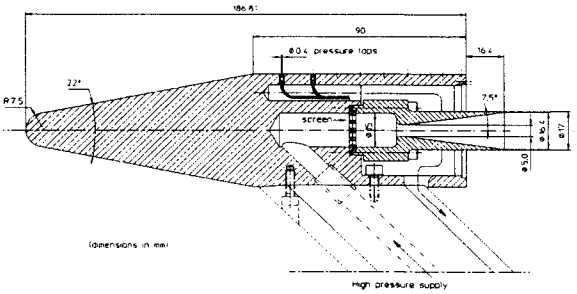

Fig 1: Blunt cone-cylinder configuration showing exhaust nozzle and construction details.

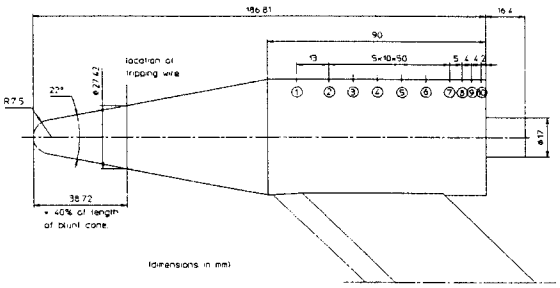

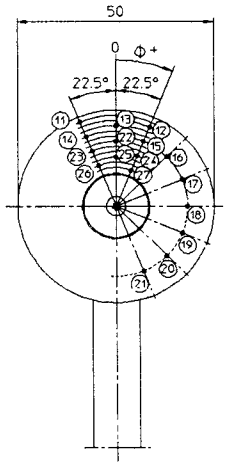

Fig 2: Location of pressure taps along cylindrical afterbody and at the base.

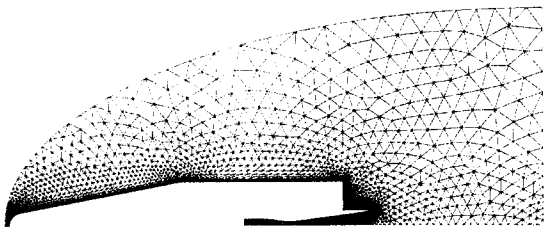

Fig 3: Unstructured coarse grid, 15,505 nodes (MDU code).

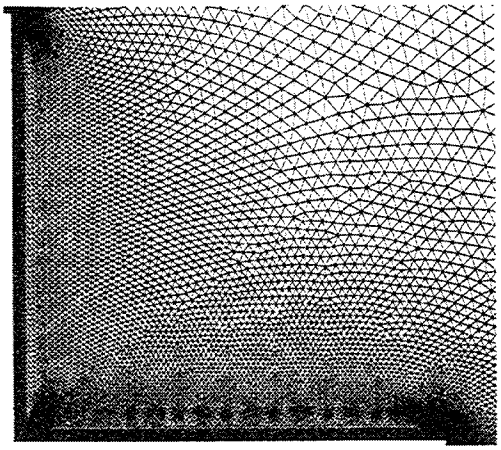

Fig 4: Unstructured fine grid in base region, 119,519 nodes (MDU code).

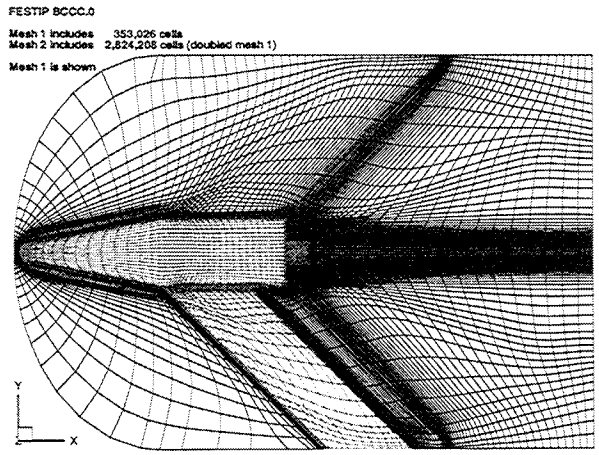

Fig 5: Three-dimensional coarse grid (mesh 1), 353,026 cells (LORE code).

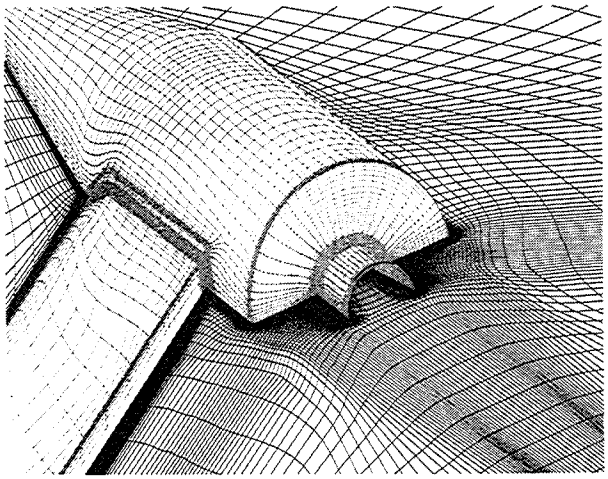

Fig 6: Three-dimensional coarse grid (mesh 1) near base (LORE code).

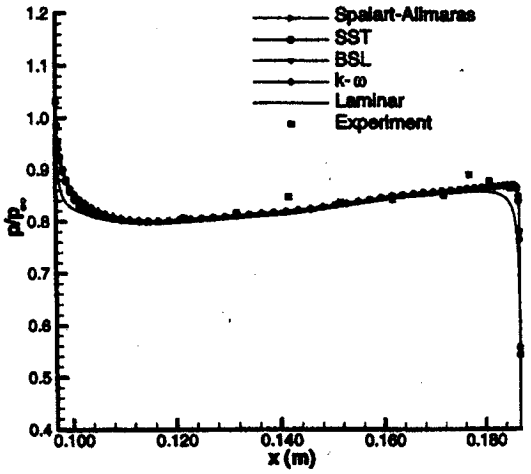

Fig 7: Pressure distribution along cylindrical afterbody computed with MDU code.

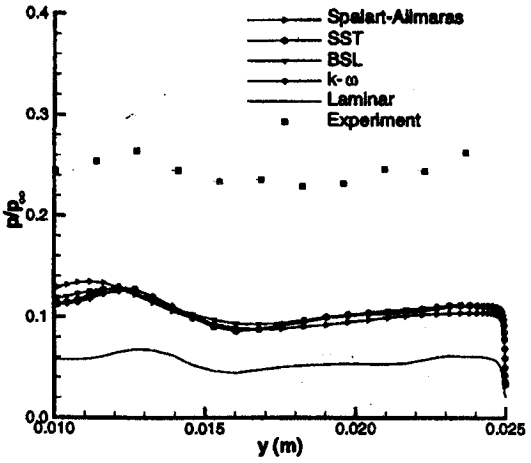

a) coarse grid

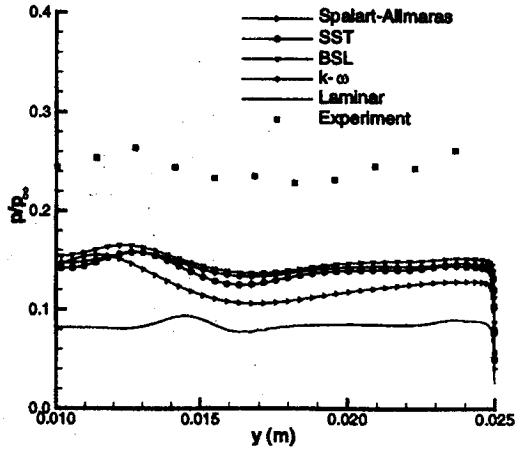

b) fine grid

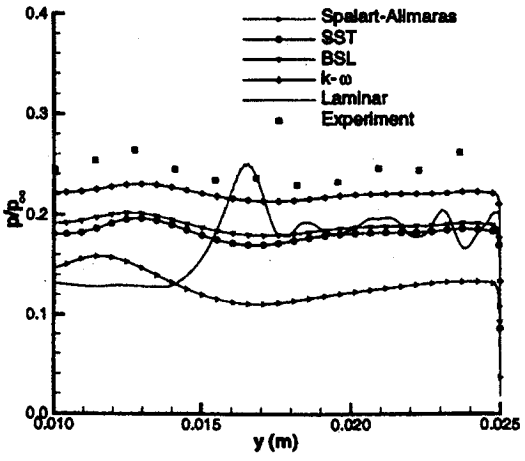

c) very fine grid

Fig 8a, b, c: Radial base pressure distribution computed with MDU code.

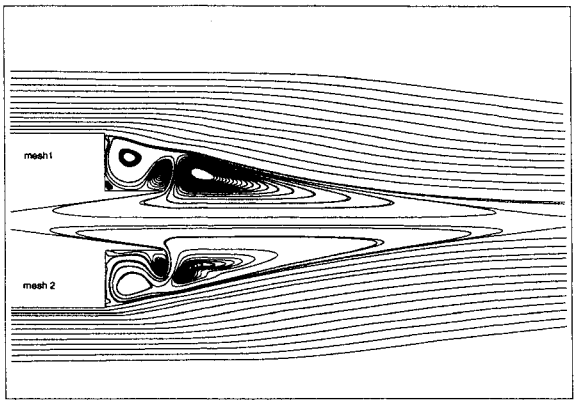

a) Laminar flow

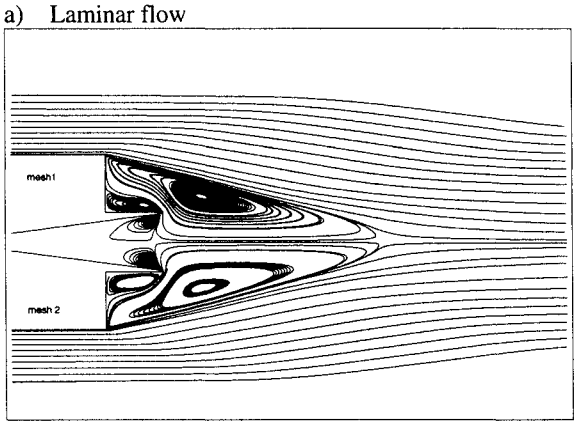

b) k-ω

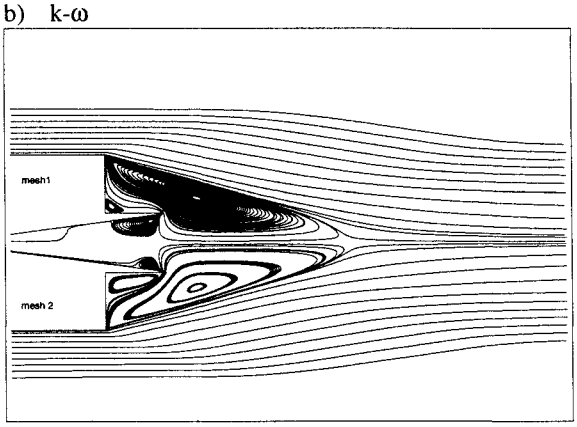

c) SST-0

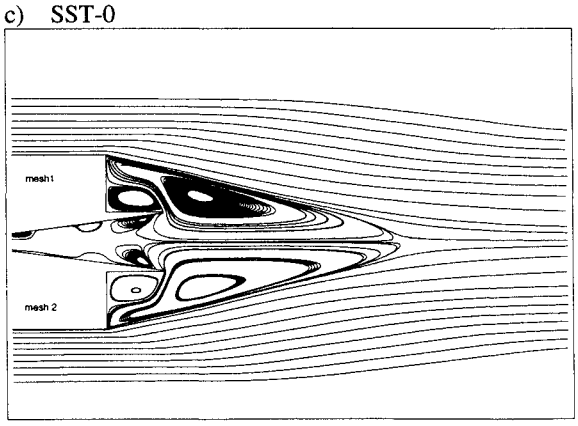

d) SST-1

Fig 9 a,b,c,d: Axisymmetric base flow computed with LORE code on grids, mesh 1 = coarse mesh and mesh 2 = fine mesh; $M_\infty = 2.98$, plume off.

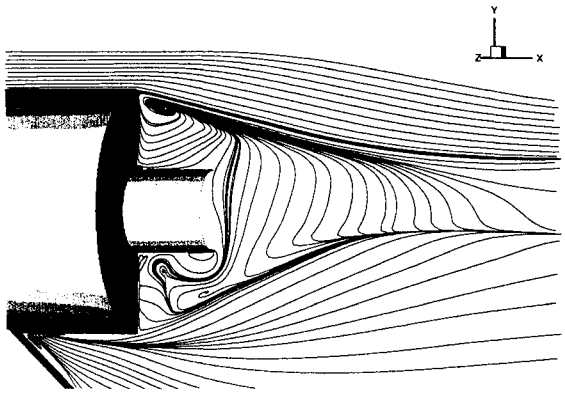

a) Laminar flow

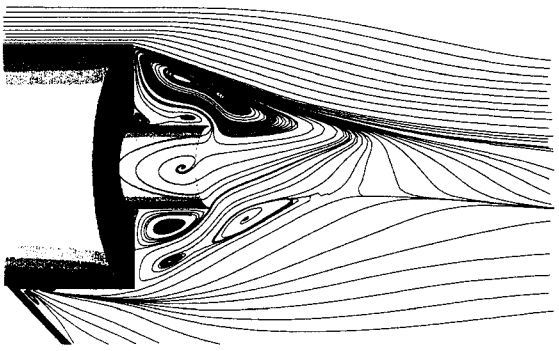

b) k-ω

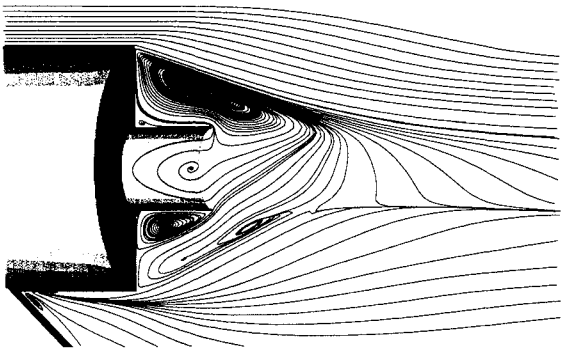

c) SST-0

d) SST-1

Fig 10 a,b,c,d: Three-dimensional base flow topologies computed with LORE code on coarse grid (mesh 1); $M_\infty = 2.98$, plume off.

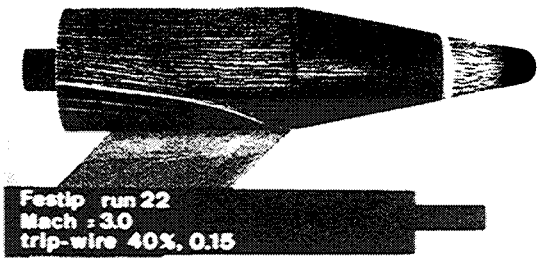

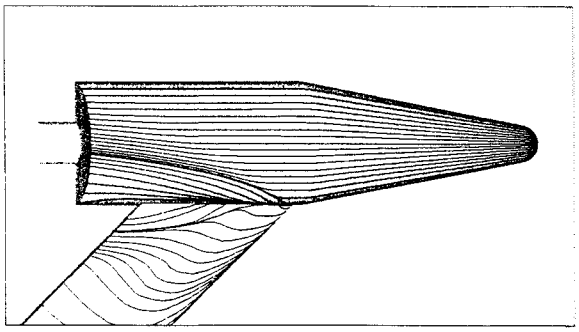

Fig 11: Comparison of computational surface shear stress lines on 3-D configuration (coarse grid, SST-1 turb. mod.) with experimental oil streak lines; M_∞ = 2.98, plume off.

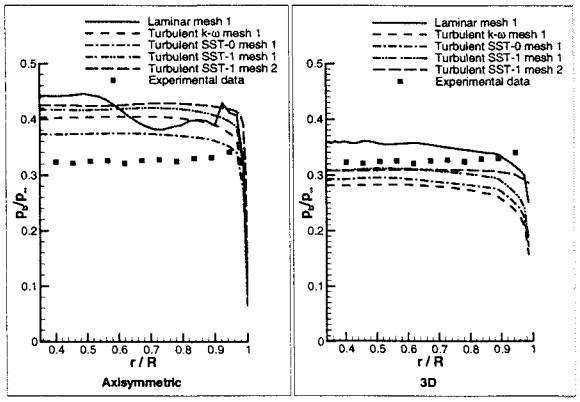

Fig 12: Radial base pressure distribution for plume-off case at M_∞ = 2.98.

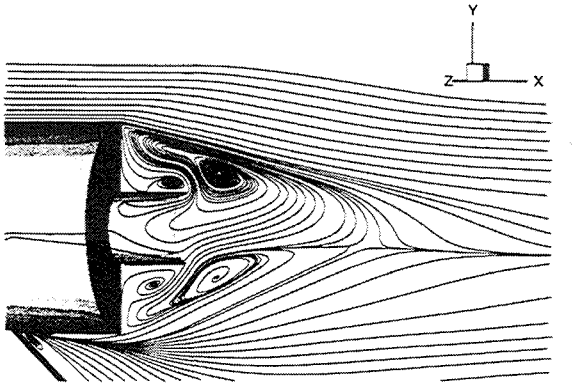

a) No plume

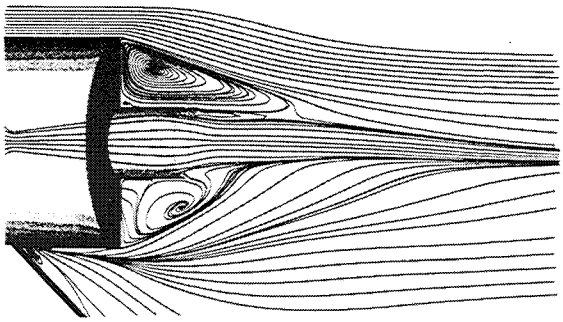

b) N=12.9

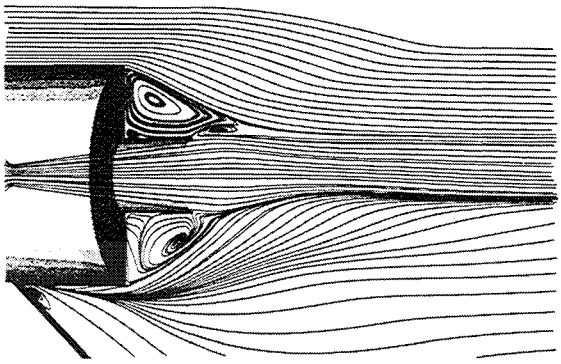

c) N=44.0

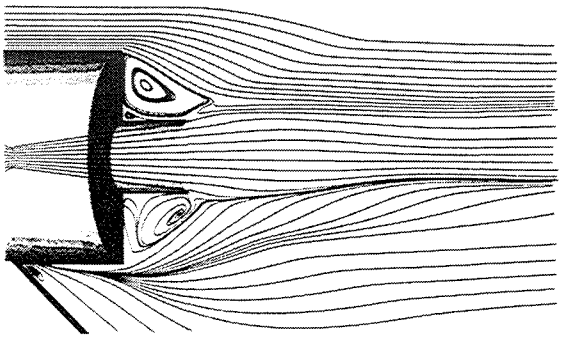

d) N=173.9

Fig 13 a,b,c,d: Three-dimensional base flow topologies for turbulence model SST-1 at different jet stagnation pressures and at M_∞ = 1.96.

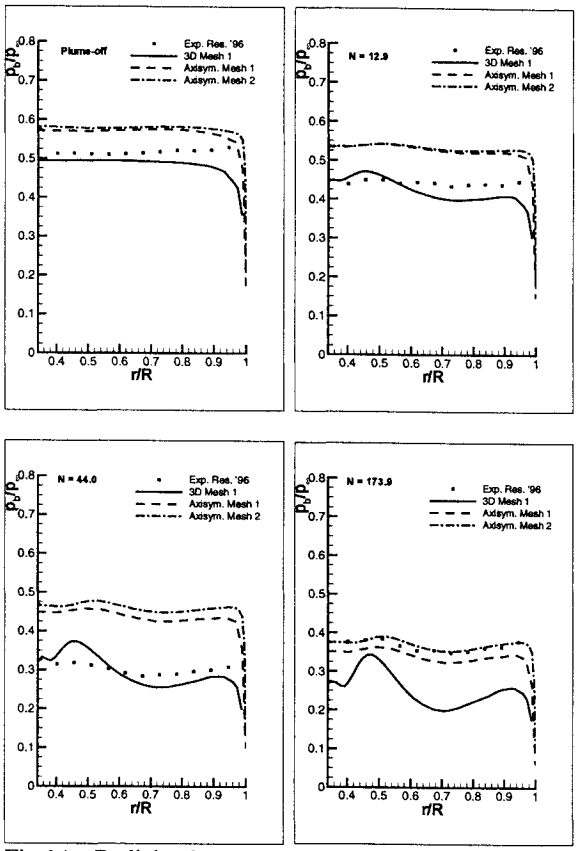

Fig 14: Radial base pressure distribution for turbulence model SST-1 at different jet stagnation pressures and at $M_\infty = 1.96$.

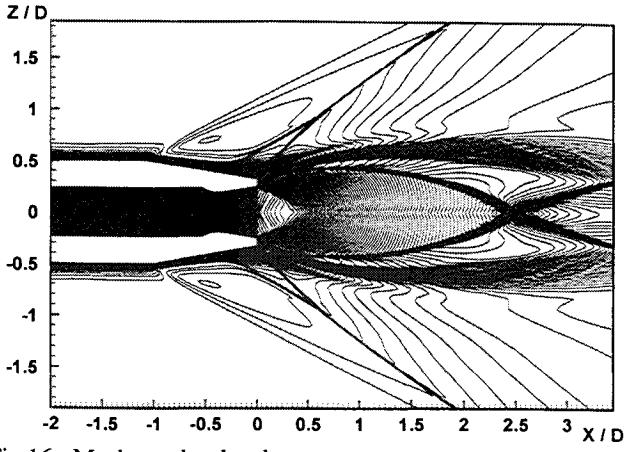

Fig 16 : Mach number levels.

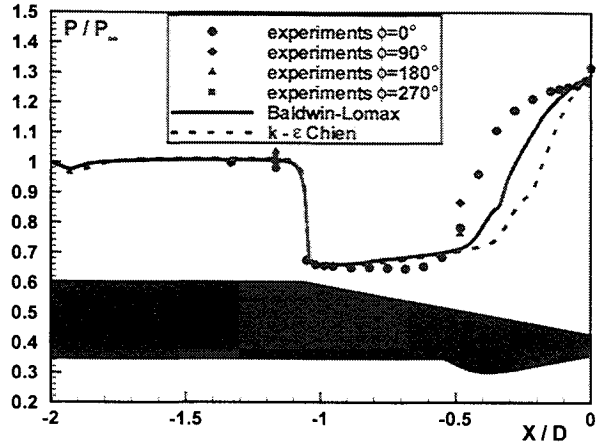

Fig 17 : Boattailed afterboby wall pressure profiles.

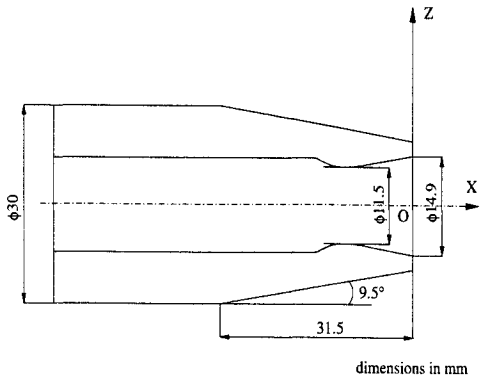

Fig 15 : Boattailed afterbody geometry.

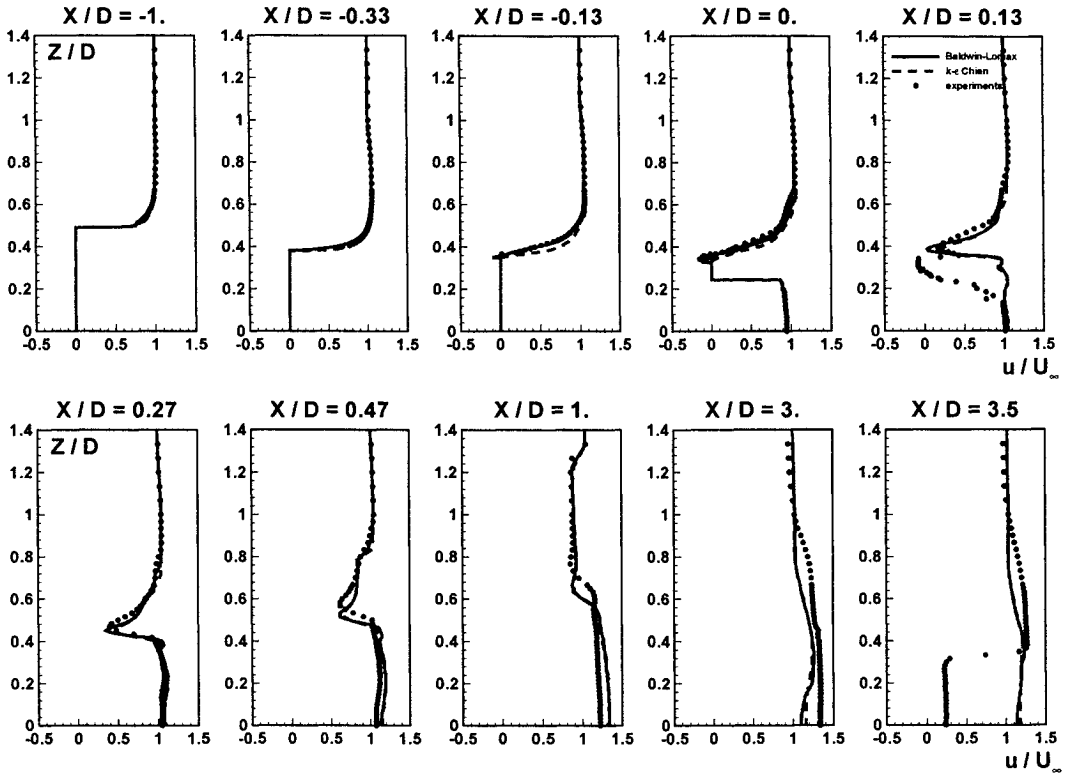

Fig 18 : Axial velocity profiles.

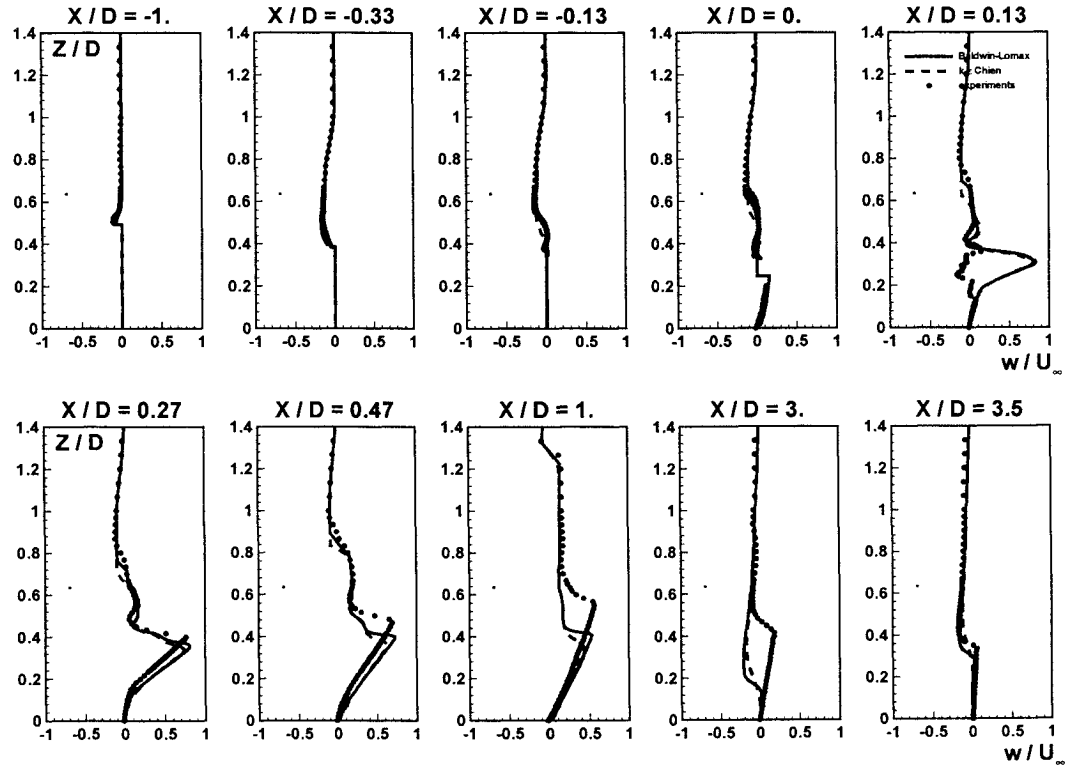

Fig 19 : Radial velocity profiles.

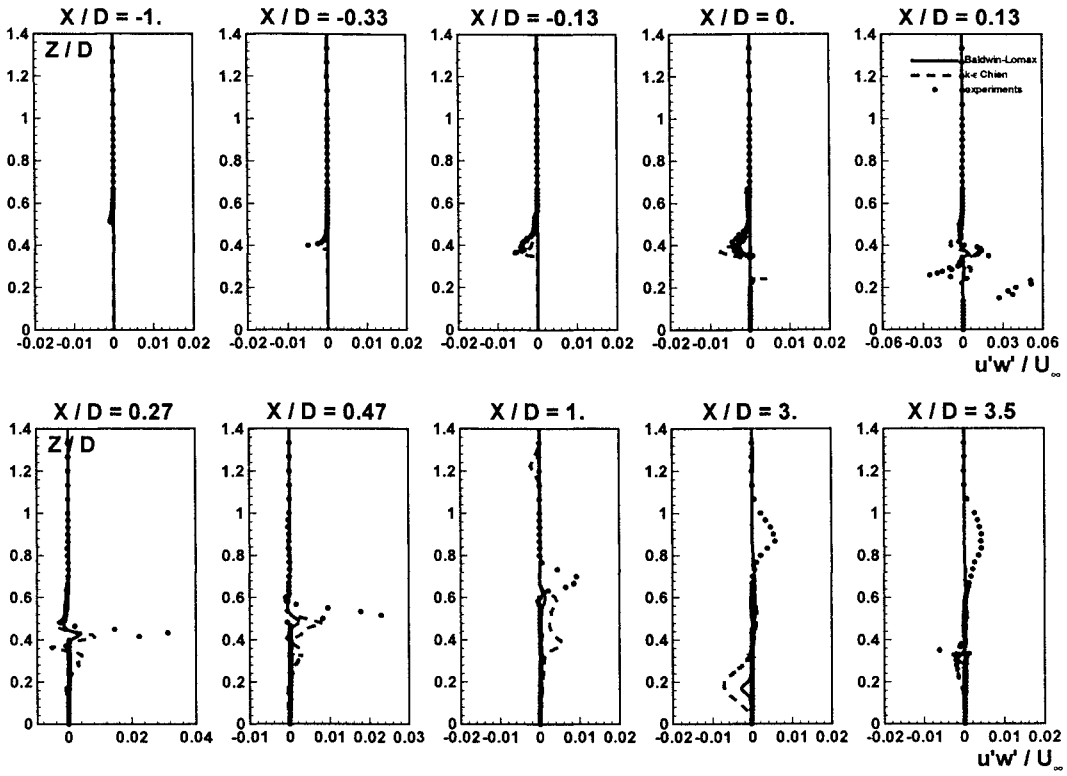

Fig 20 : Turbulent shear stress profiles.